

Frequency Comb Enhancement via the Self-Crystallization of Vectorial Cavity Solitons

Graeme N. Campbell^{1,2,*}, Lewis Hill², Pascal Del'Haye^{2,3}, and Gian-Luca Oppo¹

¹*SUPA and Department of Physics, University of Strathclyde, Glasgow, G4 0NG, Scotland, UK*

²*Max Planck Institute for the Science of Light, 91058 Erlangen, Germany*

³*Department of Physics, Friedrich-Alexander-Universität Erlangen-Nürnberg, 91058 Erlangen, Germany*

Long range interactions between dark vectorial temporal cavity solitons are induced through the spontaneous symmetry breaking of orthogonally polarized fields in ring resonators. Turing patterns of alternating polarizations form between adjacent solitons, pushing them apart so that a random distribution of solitons along the cavity length reaches equal equilibrium distances. Enhancement of the frequency comb is achieved through the spontaneous formation of regularly spaced soliton crystals, ‘self-crystallization’, with greater power and spacing of the spectral lines for increasing soliton numbers.

The generation of optical frequency combs [1] is an active area of research due to the wide range of practical applications that span across various fields including telecommunication [2, 3], spectroscopy [4, 5] and quantum technologies [6]. Temporal cavity solitons (TCS) [7] can be key elements for broadband optical frequency combs [8]. TCS are a special class of cavity solitons that originate in dissipative optical resonators under the action of external driving, diffraction [9, 10] and/or group velocity dispersion. Ring resonator geometries are now regularly used for the generation of optical frequency combs via TCS [1].

We consider a high finesse ring resonator composed of a Kerr medium, see Fig. 1, in the normal dispersion regime. A linearly polarized driving laser is coupled into the cavity, such that the intracavity fields may be resolved into components of orthogonal polarizations. In considering polarization components, vectorial TCSs display features in addition to those seen for a cavity with a single field, due to the possibility of spontaneous symmetry breaking (SSB) between polarization components [11]. The SSB of light within Kerr resonators has been demonstrated theoretically and experimentally where the intracavity field is composed of orthogonal polarized components [12–20], counterpropagating components [21–29], a combination of the two [30–32], and most recently, between two, or more, coupled resonators [33–36].

We investigate the polarization properties of vectorial dark cavity solitons (VDS) in the normal dispersion regime and its effects on the formation of frequency combs. In particular, we present a useful ‘self-crystallization’ phenomenon in which an initially random distribution of VDSs spontaneously form a regular soliton crystal (RSC). Previously, the generation of RSCs has been demonstrated through perturbations introduced near avoided mode crossings [37], or an external modulation [38] of the field. Here we instead present long range interactions between adjacent VDSs via a SSB of Turing patterns described by the coupled Lugiato-Lefever equations (LLE) [12, 13, 26, 39–42]

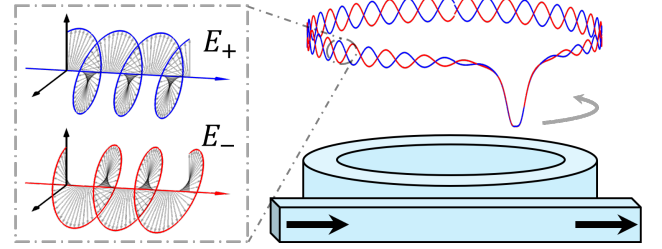


FIG. 1. A ring resonator composed of a Kerr nonlinear medium. Linearly polarised light is coupled in and out of the resonator via a waveguide. An example intracavity power profile of a vectorial soliton is shown, presenting a Turing pattern of broken symmetry between fields of opposite circular polarization, visible as out-of-phase oscillations in the background of the dark soliton pulse.

tions (LLE) [12, 13, 26, 39–42]

$$\partial_t E_{\pm} = S - (1 + i\theta)E_{\pm} + i(|E_{\pm}|^2 + 2|E_{\mp}|^2)E_{\pm} - i\partial_{\tau}^2 E_{\pm}, \quad (1)$$

where $E_{\pm}(\tau, t)$ are the slowly varying amplitudes of the two orthogonal polarization components of the field, S is the amplitude of the input field, considered to be real and positive, and θ is the input pump detuning to the near nearest cavity resonance. t is the ‘slow time’ temporal variable describing the evolution over many round trips of the cavity, while τ is the ‘fast time’ longitudinal variable describing the evolution over a single round trip of the cavity in the normal dispersion case with $0 \leq \tau \leq \tau_R$, where τ_R is the resonator round trip. Eqs. (1) are invariant under the exchange of the $+$ and $-$ indices, the fundamental symmetry of the system. Stationary solutions satisfying $E_+ = E_-$ are symmetric and $E_+ \neq E_-$ are symmetry broken.

We first provide a description of the SSB of the homogeneous stationary solutions (HSS) of Eqs. (1). The HSS of Eqs. (1) correspond to the two coupled equations

$$S^2 = H_{\pm}^2 - 2(\theta - 2H_{\mp})H_{\pm}^2 + ((\theta - 2H_{\mp})^2 + 1)H_{\pm}, \quad (2)$$

where $H_{\pm} = |E_{0,\pm}|^2$ is the power of the HSS $E_{0,\pm}$. In

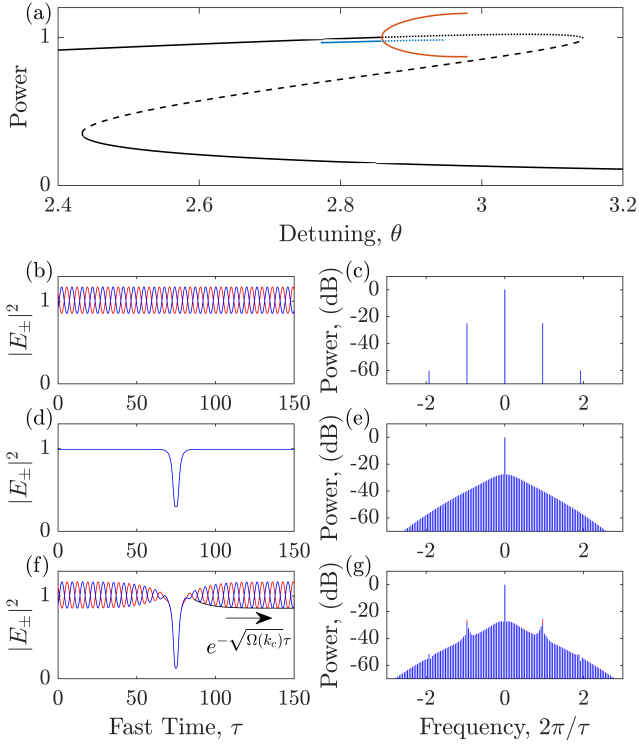


FIG. 2. Solutions of Eqs. (1) for $S = 1.01, \tau_R = 150$. (a) Stable (solid black curves) and unstable (broken black curves) symmetric homogeneous solutions, and stable (solid blue curves) and unstable (broken blue curves) symmetric single dark soliton solutions plotted as their average power. The maximum and minimum power of stable symmetry broken Turing pattern are also shown, in red. (b) Turing pattern of alternating polarization for $\theta = 2.94$ and (c) the corresponding frequency comb. (d) Power profile of symmetric dark soliton solutions for $\theta = 2.8$ and (e) the corresponding frequency comb. (f) Power profile of symmetry broken dark soliton solutions for $\theta = 2.94$ and (g) the corresponding frequency comb. The black curve in (f) outlines the envelope of the Turing pattern $\propto \exp(-\sqrt{\Omega(k_c)}\tau)$ as it approaches the vectorial dark soliton.

Fig. 2a we plot solutions of Eq. (2) for $S = 1.01, \tau_R = 150$. For this value of S there are only symmetric HSS ($H_+ = H_-$) which are plotted as the black curve. In the parameter region of our interest there are no symmetry broken HSS solutions. The symmetric HSS form a tilted Lorentzian curve, where stable solutions are plotted with solid lines and and unstable solutions as broken lines. We note that Eqs. (1) have undergone extensive investigation in the absence of fast time effects [12, 25, 26, 43].

Of key importance here is a Turing instability due to a SSB bifurcation of the high power bistable symmetric HSS typical of regimes of normal dispersion, resulting in the formation of a Turing pattern stationary state formed of alternating orthogonal polarizations. This supercritical bifurcation occurs when increasing the detuning and is plotted as a red curve depicting the maximum

and minimum powers of the Turing pattern in Fig. 2a. This instability is due to the field interaction through the cross-Kerr modulation and so it is not present on the high power HSS of a single LLE [44, 45]. The Turing instability is found by considering perturbations on the HSS of the form $E_{\pm} = E_{0,\pm} + \epsilon_{\pm} e^{ik\tau + \Omega t}$ where k is the wavenumber of the perturbation and Ω is the slow time eigenvalue. The growth rate of this perturbation is then

$$\Omega(k) = -1 \pm \sqrt{\frac{-A_1 B_1 - A_2 B_2 \pm Q}{2}}, \quad (3)$$

$$Q = \sqrt{(A_1 B_1 - A_2 B_2)^2 + 4A_1 A_2 C^2}, \quad (4)$$

where $A_{1,2} = \theta - k^2 - H_{\pm} - 2H_{\mp}$, $B_{1,2} = \theta - k^2 - 3H_{\pm} - 2H_{\mp}$, $C^2 = 8H_+ H_-$. These eigenvalues have a similar form to the linear stability analysis of Refs. [25, 26] where dispersion is neglected ($k = 0$). From these eigenvalues we may approximate the Turing wavenumber from the critical wavenumber with largest growth, $\Omega(k_c)$. For the example Turing pattern shown in Fig. 2b we find a good agreement between the predicted $k_c \approx 0.96$ and measured $k \approx 1.01$ wavenumber, although the value of θ is well above the Turing instability threshold.

In the normal dispersion regime, Eqs. (1) exhibits VDSs [44]. These solutions are composed of localized switching fronts which connect the high and low power stable HSSs. Oppositely oriented pairs of switching fronts can ‘lock’ due to the interaction of local fast time oscillations close to the lower power plateau and become stationary VDS. This mechanism of soliton formation was first proposed for spatial solitons composed of diffractive switching fronts [46–48], but has been demonstrated longitudinally in the ring resonator with a single field component theoretically [44] and experimentally [49], as well as in Fabry-Pérot configurations [50].

First considering symmetric solitons, we note that at symmetry $E_+ = E_- = E$, Eqs. (1) reduce to

$$\partial_{\tau} E = S - (1 + i\theta)E + 3i|E|^2 E - i\partial_{\tau}^2 E. \quad (5)$$

This means that under a re-normalization of fields $E \rightarrow E/\sqrt{3}$, $S \rightarrow S/\sqrt{3}$ the stationary VDS of our system are analogous to those of the LLE. A branch of symmetric solutions of Eqs. (1) containing a single VDS is shown in 2a as the blue curve (plotted as the average power over a round trip to separate it from the HSS). At this parameter value ($S = 1.01$) symmetric VDSs are stable for values of detuning below the Turing instability, shown in Fig. 2d-2e. As the detuning is increased, the VDS symmetric solution undergoes a SSB of the homogeneous background from which the soliton hangs. This SSB results in the formation of a Turing pattern of alternating polarization components and is phenomenologically identical to the SSB of the HSS in the absence of the VDS.

The frequency comb of a symmetry broken VDS is shown in Fig. 2g. It maintains a similar spectral envelope

to that of the single symmetric VDS (Fig. 2e) but it develops sidebands due to the periodic modulations at the tails. The sideband peaks are reminiscent of those generated by dispersive waves due to higher order dispersion [51]. Here they are achieved with second order dispersion and the contribution of the Turing pattern modulation. The power and separation of these peaks correspond to the spectral lines of the frequency comb of the Turing pattern, Fig. 2c.

An important property of symmetry broken VDSs is that the amplitude of the Turing pattern envelope decays as $[\exp(-\sqrt{\Omega(k_c)}\tau)]$, with $\Omega(k_c)$ given by Eq. 3, from the place where the VDS tails are close to the unstable symmetric HSS to a saturation value of the modulated intensity. The black line in Fig. 2f shows this exponential decay matching the Turing pattern minima at the tails of the VDS. We have verified that such agreement persists over a wide range of detunings and input pumps where symmetry broken VDS are found.

We now consider solutions containing multiple VDSs along the cavity length simultaneously. After the SSB bifurcation, such solutions form Turing patterns in the intervals between VDSs. As the Turing patterns grow, adjacent VDS are ‘pushed’ apart until an equilibrium of the pattern’s amplitude is reached on both sides of the VDS, as shown in Fig. 3. The formation of the symmetry broken Turing pattern is hence found to introduce long range repulsive interaction between adjacent VDSs. Note that the symmetric VDSs do not exhibit these long range interactions and the VDSs remain stationary at arbitrary separation distances.

In Fig. 3a we start with three symmetric VDSs randomly distributed along the round trip for $S = 1.02$, $\theta = 2.94$ and $\tau_R = 150$. For these parameter values, the homogeneous background is unstable to the formation of Turing pattern of alternating polarizations. The maximum amplitude reached by the Turing patterns in the intervals separating the VDSs depends on the separation of adjacent VCSs. As the pattern amplitude grows, the VDS are ‘pushed’ along the resonator until an equilibrium configuration of the pattern is reached on either side of each VDS. The slow time evolution of the three VDSs is shown in Fig. 3c through direct numerical integration of Eqs. (1). Here it can be seen that the VDSs move such as to spread out along the cavity coordinate. This evolution ends in the stationary state shown in Fig. 3d composed of VDSs located equidistantly on the round trip of the cavity and separated by Turing patterns equal amplitude, thus forming a perfect soliton crystal.

The formation of such a RSC induced by SSB evolves spontaneously from the initial condition of three randomly positioned dark solitons. The organization process corresponds to self-crystallization from a random distribution of VDSs. The RSCs of our system are robust to a change in the number of VDS as the repulsive interaction will redistribute VDS to equidistant locations, as long as

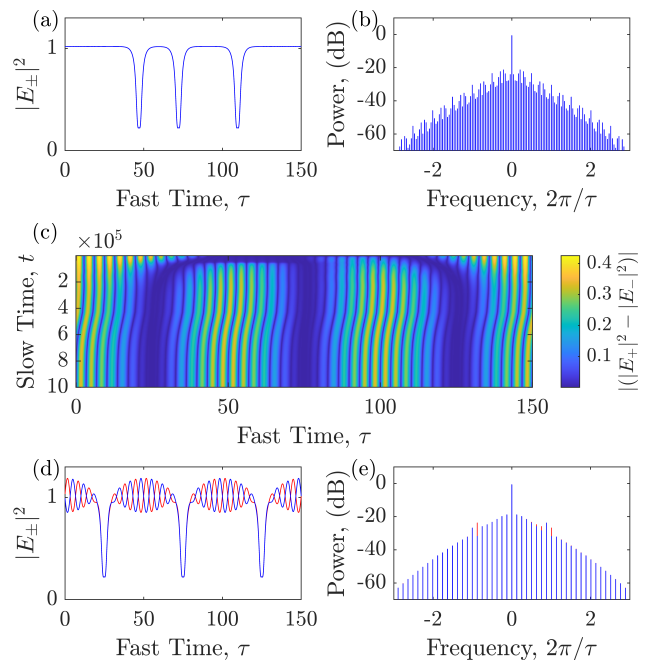


FIG. 3. Evolution of three symmetry broken vectorial dark solitons for $S = 1.02$, $\theta = 2.91$. Starting from an equal field condition (a), VDSs undergo SSB and move through the cavity as shown in (c), finally reaching a the RSC stationary state (d). Frequency combs corresponding to a random distribution of VDS (the initial condition shown in 3a) and a symmetry broken RSC (the final state shown in 3c) are presented in (b) and (e) respectively.

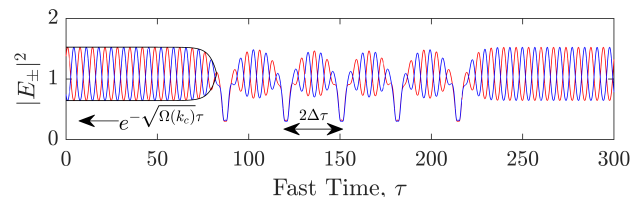


FIG. 4. Partial soliton crystal composed of five VDSs for $S = 1.06$, $\theta = 3$. The VDS can move no closer than $2\Delta\tau$ due to the repulsive interactions induced by the Turing pattern. The black curve follows the Turing pattern envelope starting from full saturation towards the VDS.

the new RSC spacing is shorter than twice the characteristic Turing patterns saturation length $\Delta\tau$, defined as the fast time distance where the pattern amplitude reaches its maximum value.

As can be seen in Fig. 3e, the RSC produces a frequency comb with a smooth spectral envelope and a spectral range three times larger than the frequency comb of the initial condition shown in Fig. 3b. In general, a RSC composed of N VDSs produces a frequency comb equivalent to a single VDS in a cavity with round trip τ_R/N . The RSCs emulate smaller cavity sizes, such that with increasing soliton number, a frequency comb with

enhanced power and greater spacing of the spectral lines is obtained. Due to these features, the spontaneous formation of RSC has many potential applications, such as satellite communications [52], photonic radar [53] and radio-frequency filters [54, 55]. Being a self-organized structure, the RSC of our system offer different ways to generate and control RSCs than those demonstrated in Refs. [37, 38]. As mentioned earlier, regular peaks in the spectral envelope are due to the Turing pattern wavenumber that is required for self-crystallization. Such peaks can be removed at will after self-crystallization by changing the control parameters across the SSB bifurcation, thus leaving a symmetric RSC with no pattern states between the VDS.

Even in the case of a small number of VDSs in a long cavity, such as in Fig. 4, VDSs are found to move apart until a saturation of the Turing pattern amplitude is reached in the interval between them. In Fig. 4, five VDSs have undergone SSB, and spread apart until the VDSs become stationary and produced a local RSC via self-crystallization. The maximum range of the repulsive interaction between VDSs can be investigated using the growth rate, Eq. 3, of the critical wavenumber k_c of the Turing pattern away from the VDS. We are able to estimate the a maximum interaction distance $2\Delta\tau \approx -2\ln(0.01|E_{\max}|^2)/\sqrt{\Omega(k_c)}$, where we have assumed the VDS interaction disappears when the Turing amplitude reaches 1% from the maximum amplitude $|E_{\max}|^2$. This predicts a maximum lattice spacing of $2\Delta\tau \approx 32$ compared to the measured $2\Delta\tau \approx 30$ from Fig. 4. The interaction distance of VDSs can then be controlled by changing the control parameters to alter the growth rate of the Turing patterns. A pair of VDSs will no longer interact should their separation be greater than $2\Delta\tau$ where the mediating Turing patterns reach saturation. By selecting a suitable cavity length and soliton number such that $N > \tau_R/2\Delta\tau$ we observe the self-crystallization phenomenon as is shown in Fig. 3.

RSCs are composed of a unit cell which is perfectly repeating over the cavity round trip. The example RSC of Fig. 3d is composed of the unit cell shown in Fig. 5a repeated three times over the round trip. This solution is bistable with the RSC composed of the unit cell shown in Fig. 5b. These two unit cells possess the fast time symmetries $E_{\pm}(-\tau) = E_{\mp}(\tau)$ and $E_{\pm}(-\tau) = E_{\pm}(\tau)$ respectively, and two additional unit cells obtained by exchanging the fields $E_+ \leftrightarrow E_-$ in Fig. 5. As such, there are four possible RSCs, each related by an integer multiple phase shift of $\pi/2$ in the peaks of the Turing pattern. We find that all four RSCs are stable and can be reached depending on the initial condition.

If we return to Fig. 3 we see that the evolution of the three VDSs is composed of two regimes. For slow time $t < 3 \times 10^5$, the VDSs move apart due to the formation of the Turing patterns. At slow time $t \approx 3 \times 10^5$, the three VDSs approach an equal spacing in the cavity, but

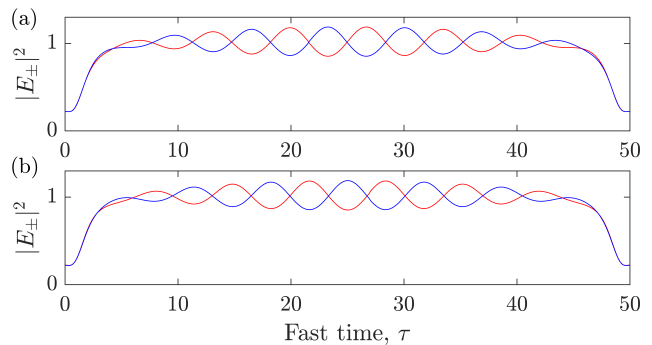


FIG. 5. (a)-(b) Power profiles of RSC unit cells for $S = 1.02, \theta = 2.91, \tau_R = 50N$. Two additional unit cells can be obtained by exchanging the fields $E_+ \leftrightarrow E_-$ in both (a) and (b). The unit cells are related by a phase shift in the peaks of the Turing patterns of $\pi/2$.

here the Turing pattern displays a non integer $\pi/2$ phase shift with respect to the stationary unit cells presented in Fig. 5. We now see transient dynamics in which the equidistant VDSs lattice and Turing pattern drift in fast time at different rates. This drift continues until one of the four stationary configurations is reached. We note the possibility of forming ‘defective’ crystals composed of alternating combinations of these four unit cells, which we leave for future publications.

In conclusion, the formation of a RSC is achieved from a random distribution of VDSs via pattern formation with two field components of orthogonal polarization. SSB results in the formation of Turing patterns of alternating polarization at the tails of the VDSs. Long range interactions between VDSs are induced and mediated by Turing patterns, which increase the separation between adjacent VCSs until an equidistant equilibrium distance is reached and a regularly spaced soliton crystal is formed. The growth of Turing patterns can be controlled by changing the control parameters, which determine the range of the interaction. Above the Turing instability, RSCs originate spontaneously (self-crystallization) without the need of any perturbation [37, 38] and represents a new, readily implementable, method for RSC formation relevant for application [52–55]. RSCs produce a frequency comb displaying a smooth spectral profile and increased line spacing when compared to a random distribution of cavity solitons. As such, a RSC may be used to emulate smaller cavity sizes while avoiding the experimental limitations of small diameter ring resonators. The self-crystallization mechanism is universal in systems displaying temporal cavity solitons and Turing instabilities and has already been generalized to Fabry-Pérot configurations with two orthogonal polarizations [30].

We acknowledge support from the EPSRC DTA Grant No. EP/T517938/1. P.D. acknowledges support by the European Union’s H2020 ERC Grant “CounterLight”

756966 and the Max Planck Society. LH acknowledges support from the SALTO scheme of the Max-Planck-Gesellschaft (MPG) and the CNRS.

* graeme.campbell.2019@uni.strath.ac.uk

- [1] A. Pasquazi et al., Micro-combs: A novel generation of optical sources, *Phys. Rep.* **729**, 1–81, (2018).
- [2] J. Pfeifle, et al., Coherent terabit communications with microresonator Kerr frequency combs, *Nat. photonics* **8**, 375–380, (2014).
- [3] J. Pfeifle et al., Optimally coherent Kerr combs generated with crystalline whispering gallery mode resonators for ultrahigh capacity fiber communications, *Phys. Rev. Lett.* **114**, 093902, (2015).
- [4] M.-G. Suh et al., Microresonator soliton dual-comb spectroscopy. *Science* **354**, 600–603, (2016).
- [5] A. Dutt et al., On-chip dual-comb source for spectroscopy, *Science advances*, **4**, e1701858, (2018).
- [6] Christian Reimer et al., Generation of multiphoton entangled quantum states by means of integrated frequency combs, *Science*, **351**, 1176–1180, (2016).
- [7] S. Coen and M. Erkintalo, Temporal cavity solitons in Kerr media, in *Nonlinear optical cavity dynamics: from microresonators to fiber lasers* edited by P. Grelu (John Wiley & Sons, New York, 2015), pp. 11–40.
- [8] T. J. Kippenberg, R. Holzwarth, and S. A. Diddams, Microresonator-based optical frequency combs, *science*, **332**, 555–559, (2011).
- [9] A. J. Scroggie et al., Pattern formation in a passive Kerr cavity. *Chaos, Solitons & Fractals*, **4**, 1323–1354, (1994).
- [10] W. J. Firth and A. J. Scroggie, Optical bullet holes: robust controllable localized states of a nonlinear cavity, *Phys. Rev. Lett.*, **76**, 1623, (1996).
- [11] D. N. Christodoulides and R. I. Joseph, Vector solitons in birefringent nonlinear dispersive media, *Opt. Lett.* **13**, 53–55, (1988).
- [12] B. Garbin et al., Asymmetric balance in symmetry breaking, *Phys. Rev. Res.* **2**, 023244, (2020).
- [13] Gang Xu et al., Spontaneous symmetry breaking of dissipative optical solitons in a two-component Kerr resonator, *Nat. Commun.* **12**, 4023, (2021).
- [14] G. Xu et al., Breathing dynamics of symmetry-broken temporal cavity solitons in Kerr ring resonators, *Opt. Lett.*, **47**, 1486–1489, (2022).
- [15] N. Moroney et al., A Kerr polarization controller, *Nat. Commun.* **13**, 398, (2022).
- [16] L. Quinn et al., Random number generation using spontaneous symmetry breaking in a Kerr resonator, *Opt. Lett.* **48**, 3741–3744, (2023).
- [17] S. Coen et al., Nonlinear topological symmetry protection in a dissipative system, *Nat. Commun.* **15**, 1398, (2024).
- [18] L. Quinn et al., Towards a novel coherent Ising machine using symmetry breaking in a Kerr resonator, In *AI and Optical Data Sciences IV*, page PC1243806. SPIE, (2023).
- [19] J. Fatome et al., Observation of polarization Faticons in a fibre Kerr resonator, in *Conference on Lasers and Electro-Optics/Europe (CLEO/Europe 2023) and European Quantum Electronics Conference (EQEC 2023)*, paper pd.2.7, (2023).
- [20] T. Huang et al., Coexistence of nonlinear states with different polarizations in a Kerr resonator, *Phys. Rev. A* **109**, 013503, (2024).
- [21] A. E. Kaplan and P. Meystre. Enhancement of the sagnac effect due to nonlinearly induced nonreciprocity. *Opt. Lett.* **6**, 590–592, (1981).
- [22] A.E. Kaplan and P. Meystre, Directionally asymmetrical bistability in a symmetrically pumped nonlinear ring interferometer, *Opt. Commun.* **40**, 229–232, (1982).
- [23] E. M. Wright et al., Theory of the nonlinear sagnac effect in a fiber-optic gyroscope, *Phys. Rev. A* **32**, 2857, (1985).
- [24] L. Del Bino et al., Symmetry breaking of counter-propagating light in a nonlinear resonator, *Scientific Reports* **7**, 43142, (2017).
- [25] M. T. M. Woodley et al., Universal symmetry-breaking dynamics for the Kerr interaction of counterpropagating light in dielectric ring resonators, *Phys. Rev. A* **98**, 053863, (2018).
- [26] L. Hill, et al., Effects of self-and cross-phase modulation on the spontaneous symmetry breaking of light in ring resonators, *Phys. Rev. A* **101** 013823, (2020).
- [27] M. T. M. Woodley et al., Self-switching Kerr oscillations of counterpropagating light in microresonators, *Phys. Rev. Lett.* **126** 043901, (2021).
- [28] C. Cui, L. Zhang, and L. Fan, Control spontaneous symmetry breaking of photonic chirality with reconfigurable anomalous nonlinearity, *arXiv preprint arXiv:2208.04866*, (2022).
- [29] R. D. D. Bitha et al., Bifurcation analysis of complex switching oscillations in a Kerr microring resonator, *Phys. Rev. E* **108**, 064204, (2023).
- [30] G. N. Campbell et al., Dark Temporal Cavity Soliton Pairs in Fabry-Pérot Resonators with Normal Dispersion and Orthogonal Polarizations, *CLEO/Europe and EQEC*, paper ef.p.3, (2023).
- [31] L. Hill et al., Symmetry broken vectorial kerr frequency combs from Fabry-Pérot resonators, *Commun. Phys.*, **7**, 82, (2024).
- [32] L. Hill, G.-L. Oppo, and P. Del’Haye, Multi-stage spontaneous symmetry breaking of light in Kerr ring resonators, *Commun. Phys.*, **6**, 208, (2023).
- [33] Y. Rah, and K. Yu, Demonstration of spontaneous symmetry breaking in self-modulated ring resonators, *Phys. Rev. Res.*, **6**, 013234, (2024)
- [34] K. W. Cheah et al., Spontaneous symmetry breaking of non-Hermitian coupled nano-cavities, *Research Square preprint*, (2023)
- [35] A. Ghosh et al., Four-field symmetry breakings in twin-resonator photonic isomers, *Phys. Rev. Res.* **5**, L042012, (2023).
- [36] A. Ghosh et al., Controlled light distribution with coupled microresonator chains via Kerr symmetry breaking, *arXiv preprint arXiv:2402.10673*, (2024).
- [37] D. C. Cole et al., Soliton crystals in Kerr resonators, *Nat. Photonics* **11**, 671–676, (2017).
- [38] L. Zhizhou et al., Synthesized soliton crystals, *Nat. Commun.* **12**, 3179, (2021).
- [39] L. A. Lugiato and R. Lefever, Spatial dissipative structures in passive optical systems, *Phys. Rev. Lett.* **58**,

- 2209, (1987).
- [40] M. Haelterman et al., Dissipative modulation instability in a nonlinear dispersive ring cavity, *Opt. Commun.* **91**, 401–407, (1992).
- [41] L. A. Lugiato et al., From the Lugiato–Lefever equation to microresonator-based soliton Kerr frequency combs, *Phil. Trans. R. Soc. A.* **376**, 20180113, (2018).
- [42] J. B. Geddes et al., Polarisation patterns in a nonlinear cavity, *Opt. Commun.* **111**, 623, (1994).
- [43] G. N. Campbell et al., Counterpropagating light in ring resonators: Switching fronts, plateaus, and oscillations, *Phys. Rev. A* **106**, 043507, (2022).
- [44] P. Parra-Rivas et al., Dark solitons in the lugiato-lefever equation with normal dispersion. *Phys. Rev. A* **93**, 063839, (2016).
- [45] C. Godey et al., Stability analysis of the spatiotemporal lugiato-lefever model for Kerr optical frequency combs in the anomalous and normal dispersion regimes, *Phys. Rev. A*, **89**, 063814, (2014).
- [46] N. N. Rosanov and G. V. Khodova., Diffractive autosolitons in nonlinear interferometers, *JOSA B*, **7**, 1057–1065, (1990).
- [47] G.-L. Oppo, A. J. Scroggie, and W. J. Firth, From domain walls to localized structures in degenerate optical parametric oscillators, *Journal of Optics B: Quantum and Semiclassical Optics* **1**, 133, (1999).
- [48] G.-L. Oppo, A. J. Scroggie, and W. J. Firth, Characterization, dynamics and stabilization of diffractive domain walls and dark ring cavity solitons in parametric oscillators, *Phys. Rev. E* **63**, 066209, (2001).
- [49] B. Garbin et al., Experimental and numerical investigations of switching wave dynamics in a normally dispersive fibre ring resonator, *The European Physical Journal D* **71**, 1–8, (2017).
- [50] G. N. Campbell et al., Dark solitons in Fabry-Pérot resonators with Kerr media and normal dispersion, *Phys. Rev. A* **108**, 033505, (2023).
- [51] S. Fujii and T. Tanabe. Dispersion engineering and measurement of whispering gallery mode microresonator for Kerr frequency comb generation, *Nanophotonics* **9**, 1087–1104, (2020).
- [52] J. Federici and L. Moeller. Review of terahertz and sub-terahertz wireless communications, *Journal of Applied Physics* **107**, (2010).
- [53] J. Riemensberger et al., Massively parallel coherent laser ranging using a soliton microcomb, *Nature* **581**, 164–170, (2020).
- [54] X. Xu et al., Advanced rf and microwave functions based on an integrated optical frequency comb source, *Optics Express* **26**, 2569–2583, (2018).
- [55] J. Hu et al., Reconfigurable radiofrequency filters based on versatile soliton microcombs, *Nat. Commun.* **11**, 4377, (2020).